Atmospheric Research 257 (2021) 105588

Contents lists available at ScienceDirect

Atmospheric Research

journal homepage: www.elsevier.com/locate/atmosres

The September 2019 floods in Spain: An example of the utility of satellite data for the analysis of extreme hydrometeorological events

Francisco J. Tapiador [a,*], Cecilia Marcos [a,b], Juan Manuel Sancho [b], Carlos Santos [b], José Ángel Núñez [b], Andrés Navarro [c], Chris Kummerow [d], Robert F. Adler [e]

[a] Earth and Space Sciences (ESS) Research Group, Institute of Environmental Sciences (ICAM), Department of Environmental Sciences, University of Castilla-La Mancha (UCLM), Avda. Carlos III s/n, 45071 Toledo, Spain
[b] Agencia Estatal de Meteorología (AEMET), Headquarters, C/ Leonardo Prieto, 28071 Madrid, Spain
[c] Atmospheric Physics Group (GFA), University of León, León, Spain
[d] Department of Atmospheric Science, Colorado State University, Fort Collins, CO, USA
[e] Earth System Science Interdisciplinary Center (ESSIC), University of Maryland, College Park, MD, USA

ARTICLE INFO

Keywords:
Precipitation
GPM
Hydrometeorological events
Mediterranean

ABSTRACT

Major floods in Spain in September 9–13, 2019 resulted in seven casualties and massive losses to agriculture, property and infrastructure. This paper investigates the utility of satellite data to: (1) characterize the event when input into a hydrological model, and to provide an accurate picture of the evolution of the floods; and (2) inform meteorologists in real time in order to complement model forecasts. It is shown that the precipitation estimates from the Global Precipitation Measurement (GPM) Core Observatory (GPM-CO, available since 2014) and the merged satellite estimates provide an extraordinary improvement over previous technologies to monitor severe hydrometeorological episodes in near real time. In spite of known biases and errors, these new satellite precipitation estimates can be of broad practical interest to deal with emergencies and long-term readiness, especially for semi-arid areas potentially affected by ongoing global warming. Comparisons of satellite data of the September event with model outputs and more direct observations such as rain gauges and ground radars reinforce the idea that satellites are fundamental for an appropriate management of hydrometeorological events.

1. Introduction

The floods in southeast Spain in September 2019 offer an opportunity to evaluate the role of new satellite information available from the Global Precipitation Measurement (GPM) for monitoring extreme precipitation in semiarid areas. The case is interesting by itself: while the Mediterranean climate of the region is often subject to localized high-intensity precipitation events (Berthou et al., 2018; Cattani et al., 2009; Cortès et al., 2018, 2019; Laviola et al., 2011; Llasat et al., 2014, 2016; Lorenzo-Lacruz and Coauthors, 2019; Martín-Vide and Llasat, 2018; Mora et al., 2016; Olcina Cantos et al., 2010; Ramis et al., 2009; Ravazzani et al., 2016; Romero et al., 2005, 2015), the September floods in Eastern Spain from the 9th to the 13th were especially intense. According to the official report, the storm caused severe flooding in populated areas due to the amount and persistence of the phenomenon and was responsible for 'exceptional damage.' Indeed, the episode resulted in seven casualties and massive losses to agriculture, property and infrastructure (Fig. 1). Insurance companies estimate the damage at about 19 M USD. The most affected areas were large areas of the Valencian Community, the Region of Murcia, Castilla-La Mancha and Andalusia, and areas in the south of the Community of Madrid during the final phase of the episode. In all these places a multitude of rescues had to be made and thousands of people were evacuated. Just during the storm and only in the Valencian Community, 700 buildings were affected by floods (about 1500 dwellings) of which 150 suffered serious damage.

This paper addresses the utility and added value of GPM data for near real time monitoring of the September flood in Spain. On a wider scope, the paper reflects on the current and future use of satellite information for the management of these extreme events. Prior research on the use of satellite data for nowcasting and monitoring of hydrometeorological extremes includes (Champagne et al., 2014; De Coning, 2013; Di Paola et al., 2014; Kolios and Feidas, 2013; Neiman et al., 2012; Toté et al., 2015; van der Veen, 2012; Zhou et al., 2014; Zhuge et al., 2011).

* Corresponding author.
E-mail address: francisco.tapiador@uclm.es (F.J. Tapiador).

https://doi.org/10.1016/j.atmosres.2021.105588
Received 31 August 2020; Received in revised form 24 February 2021; Accepted 21 March 2021
Available online 27 March 2021

Fig. 1. Some local impacts of the flashfloods over populated areas in the Segura river basin. Credits: F. J. Ortiz Zaragoza (upper left) and Rate Bas and Vegabajadigital (rest of the photographs).

Since the launch of the GPM Core Observatory (GPM-CO) in 2014, the GPM constellation has consolidated its role as a main reference for accurate and timely estimation of precipitation for the whole planet. Products such as the IMERG (Huffman et al., 2018a; Huffman et al., 2018b), which provides 30 min accumulations with short latency through a combination of sources are widely used by the community (Asong et al., 2017; Dezfuli et al., 2017; Gaona et al., 2016; Lu and Yong, 2018; Retalis et al., 2018; Watters et al., 2018). These estimates can not only be combined with hydrological models, but also be used in near real time thanks to the low latency of the products. The GPM-CO's GPM Microwave Imager (GMI, 23 min average latency), the Dual Precipitation Radar (DPR, 76 min average), the combined GMI + DPR (83 min average) and IMERG multi-satellite estimates (5 h average for the 'early' product) are all, in principle, suitable for a variety of near real time applications (Belabid et al., 2019; Kirschbaum and Stanley, 2018; Lin et al., 2015; Mastrantonas et al., 2019; Pu et al., 2019; Yuan et al., 2017).

2. Data and methods

Information available in near real time for the management of the September 2019 floods in Spain included: Radar (Section 2.1 below); Rain gauges (2.1); Infrared-derived precipitation estimates (2.2); Microwave-based precipitation estimates (2.2); High spatial-resolution visible (VIS) imagery (2.2); Numerical Weather Prediction (NWP) model forecasts and ensembles of NWP models (2.3); and hydrological model outputs (2.4). Table 1 summarizes their main characteristics, which are described below.

2.1. Ground observations

The Meteorological Agency of Spain (AEMET) radar network comprises 15C-band (5.60–5.65 GHz) Doppler radars covering the Iberian Peninsula, the Balearics and the Canary Islands. Scans are done for two ranges: long-range scans up to 240 km distance at 1 km horizontal resolution, and short-range scans up to 120 km distance at 0.5 km horizontal resolution. Each instrument carries first carries out data processing and obtains reflectivity, radial velocity and turbulence fields. Then, a centralized processing system computes specific products: Plan Position Indicator (PPI), top echoes (ECHOTOP), Vertical Reflectivity Profile (VRP) and Vertical Integrated Liquid (VIL), for each radar. A national composite is then built for those radars covering the Iberian Peninsula and the Balearics. The composite is simply a mosaic of all operating radars at a given moment. The data frequency of the individual radars and the composite is 10 min.

AEMET also manages 945 weather stations recording data at 10 min intervals. The location of the stations was optimized to provide a comprehensive coverage of the country, favoring flat, agricultural, populated areas over remote mountain areas. The Segura River Basin Authority also has an automatic hydrological information system which records rainfall at 62 control points. The system consists of automatic rain meters scattered in the basin of the Segura River, which has been one of the main affected areas by the September 2019 floods. In both networks, the rain gauges have a 0.2 mm nominal resolution.

2.2. Satellite data

Since 2014, the GPM Core Observatory is a key piece for monitoring extreme precipitation events. The GPM-CO radar estimates (DPR) provides high quality precipitation estimates and helps calibrate the radiometer (the GMI) estimates, whose wider swath extends the coverage of the microwave instruments. The IMERG is produced by integrating the data from other satellites of the Precipitation Measuring Missions

Table 1
Data used in the study, summarizing their main characteristics.

Data source	Description	Spatial resolution	Temporal resolution	Use/notes
National radar composite	Fifteen C-band Doppler radars	1 km	10 min	Qualitative evolution of precipitation fields
Rain gauges	946 weather stations +62 stations (Segura river)	Pointwise	10 min	Ground truth measurements of precipitation
IMERG-Early	Satellite precipitation estimates from radar, radiometers, and model-derived motion vectors	10 km	3 h	Provides quantitative estimates beyond rain gauge locations and can help the forecasters
METEOSAT SEVIRI	Visible (VIS) and infrared (IR) data	3 km	15 min	Used for nowcasting by AEMET forecasters
Sentinel 2A	Visible (VIS) data	10 m	About 5 days	Provide high-resolution visible data for flood analysis and damage reports
HRES-IFS (ECMWF)	Numerical Weather Prediction Model	9 km	30 min (typical output)	Deterministic global model. 4D-var assimilation, likely the best available NWP model
HARMONIE-AROME	Numerical Weather Prediction Model	2.5 km	30 min (typical output)	Deterministic, limited area model nested in the HRES-IFS. 3D-var assimilation
ENS-IFS	Ensemble prediction system, IFS	9 km	30 min (typical output)	Non-deterministic
γ-SREPS	Ensemble prediction system (HARMONIE-AROME, ALARO, WRF-ARW, NMMB + IFS, ARPEGE, GSM, GFS and GEM)	2.5 km	30 min (typical output)	Multianalyses multimodel run at AEMET
ECMWF 'point rainfall product'	Model-derived probability of rainfall exceeding a threeshold	18 km	30 min (typical output)	Post-processed ECMWF product
GFMS	Hydrological model	1/8th degree	3 h	Hydrological model feed with IMERG, uses TMPA for calibration

(PMM) constellation with infrared data using model-derived cloud motion winds (Huffman et al., 2018b). The estimates can then be used or feed for hydrology (Anagnostou, 2010). Here, the "Early" IMERG product is used to feed into a hydrological model, as it is the only available for near-real time operations.

For nowcasting operations, AEMET relies mainly on data from the SEVIRI (Spinning Enhanced Visible and InfraRed Imager) onboard Meteosat Second Generation (MSG) satellites. SEVIRI provides imagery at twelve bands ranging from VIS to thermal IR wavelengths at the temporal interval of 15 min. Most of the bands are window bands providing reflectance and brightness temperatures. There are also four absorption bands, two of them located over a wide water vapor absorption band. They provide valuable information of moisture at mid and high levels of the atmosphere. Eleven bands provide information at 3 km horizontal resolution at nadir and one of them, located at VIS wavelengths, does it at 1 km.

Sentinel satellites in polar orbits provide high spatial resolution data and permit a more detailed view of hydrological impacts at the surface (Fig. 2). Sentinel 2A, with a 290 km swath width and five days temporal resolution at the equator, provides information in 13 bands at VIS and NIR wavelengths, with horizontal resolutions between 10 and 60 m.

2.3. Model outputs

The HRES-IFS (Jakob et al., 2000; Palmer, 2019) is a deterministic and hydrostatic atmospheric global circulation model developed at the European Centre for Medium-range Weather Forecasts (ECMWF). HARMONIE-AROME (Bengtsson et al., 2017) is a deterministic and non-hydrostatic atmospheric convection-resolving regional mesoscale model, developed by HIRLAM and ALADIN consortia, as described in Seity et al. (2011) and Bengtsson et al. (2017). Though both models use the spectral modeling approach their grids are different: HRES-IFS uses an octahedral O1280 grid, which allows it to go from a 16 km grid in the dynamics to a 9 km grid in the model output, while HARMONIE-AROME works in a Lambert Conformal grid at 2.5 km. The number of vertical levels below 500 hPa is also quite similar (41 and 42) as well as below 2000 m (27 and 28) in both models. Data assimilation is 4D-Var for HRES-IFS and 3D-Var for HARMONIE-AROME.

HARMONIE-AROME is run at AEMET every 3 h taking its initial and boundary conditions from HRES-IFS every hour. The physical parameterizations of the model draw from those used in the research Meso-NH (Bougeault and Mascart, 2009) model. Radiation is parameterized as in HRES-IFS cycle 32 model, surface processes use SURFEX (Masson and Coauthors, 2013), turbulence use HARATU scheme and shallow convection uses EDMF-M (Bengtsson et al., 2017). Deep convection, in contrast to the HRES-IFS, is explicitly resolved through the ICE-3 microphysical scheme (Pinty and Jabouille, 1998; Lascaux et al., 2006).

Two different ensemble prediction systems are available at AEMET: the global ENS-IFS (Molteni et al., 1996) for the synoptic scale, and the regional γ-SREPS (Frogner et al., 2019) for the mesoscale. γ-SREPS is a multianalyses multimodel run at AEMET every 12 h with 48 h range, coupling 4 mesoscale models (HARMONIE-AROME, ALARO, WRF-ARW and NMMB) with 5 global models as initial and boundary conditions (IFS, ARPEGE, GSM, GFS and GEM). It runs at a 2.5 km horizontal resolution.

We also used 'Point Rainfall', which is a new experimental post-processed ECMWF product available from April 2019. It estimates the range of likely precipitation accumulation within the ECMWF-ENS gridbox (18 × 18 km aprox.), accounting for sub-grid variability and known model biases. It provides the probabilities of precipitation point values exceeding several thresholds, as they would be measured by a rain gauge randomly located within a gridbox. The product and its rationale are described in Owens and Hewson (2018). In short, a statistics post-processing system is built by comparing the estimated values of the system with rainfall observations and taking into account 214 gridbox-weather-types. Those weather-types are defined by using the following parameters: convective rainfall fraction, total 12 h precipitation forecast, 700 hPa wind speed, CAPE and 24 h clear-sky solar radiation.

The 'Point Rainfall' product aims to improve the raw ECMWF-ENS forecasts by adding sub-grid information and by providing better and more realistic precipitation estimates, especially in convective situations. The statistics post-processing system uses one-year worth of data for training and calibration.

The Extreme Forecast Index (EFI; Lalaurette, 2003a) is also a useful tool to help foresee unusual or extreme weather events, albeit not necessarily severe ones. For a given location and time of year, the EFI

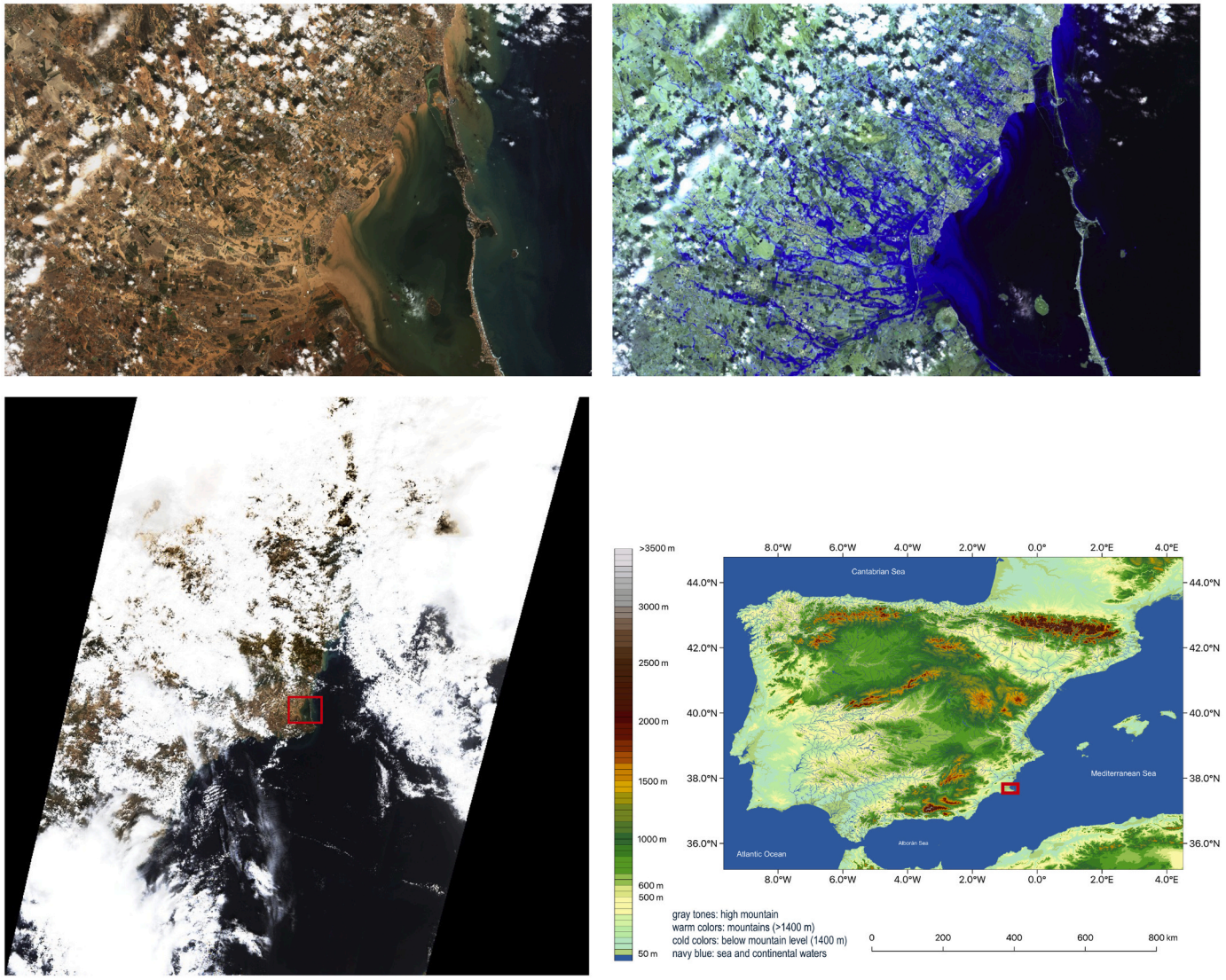

Fig. 2. (top) Sentinel 2A-L2A true color (4/3/2, left) and false color (12/11/5, right) band combinations for September 13, 2019 11:52 UTC, focused on the Mar Menor area (Murcia province). (bottom, left) Satellite swath and the area of interest, and (bottom, right) topographic map of Spain (from Tapiador et al., 2020), with the location of the main features mentioned in the paper.

identifies unusual, potentially extreme weather compared to the local climatology. It is computed as an integral measure of the difference between Cumulative Distribution Functions (CDF; Wilks, 2011) of the current ensemble forecast probability distribution and the climatology distribution, giving higher weight to differences in the tails of the distribution. In the case of ECMWF ENS-IFS the climatology is called M-climate (Zsótér et al., 2015; Owens and Hewson, 2018), and is computed considering a 5-week window centered on the target day, picking 9 fixed days for each one of the last 20 years, and reprocessing for each day an ensemble of 11 forecasts. In this way an ensemble of 1980 members called M-climate is generated. The EFI definition (Zsótér, 2006) is as follows:

$$\mathrm{EFI} = \frac{2}{\pi}\int_0^1 \frac{p - F_f(p)}{(p(1-p))^{1/2}}\,dp$$

where $F_f(p)$ denotes the proportion of ENS members lying below the p quantile of the M-climate. Those forecasts outside the M-climate are not considered (for that purpose the Shift of Tail index (SOT) is used (Lalaurette, 2003b; Zsótér, 2006). EFI values fall within the interval [−1,1]. High EFI values indicate an extreme event more likely than usual, but the actual values do not represent probabilities of that event. The interpretation is as follows: EFI = 0 where the ensemble distribution agrees precisely with the M-climate distribution, or when the overall total of positive and negative area contributions is zero, and EFI = +1 (−1) where all the ensemble values are above (below) the M-climate maximum (minimum). EFI values between 0.5 and 0.8 (irrespective of sign) generally indicate an unusual event, and values above 0.8 can signify an extreme event.

2.4. Hydrological model: the GFMS

The Global Flood Monitoring System (GFMS, http://flood.umd.edu/) is a NASA-funded system using real-time IMERG estimates as input to a quasi-global (50°N - 50°S) hydrological runoff and routing model running on a 1/8th degree resolution every 3 h (Wu et al., 2012, 2014). Flood detection and intensity estimates are based on 15 years of retrospective model runs with TRMM Multi-Satellite Precipitation Analysis (TMPA) input, with flood thresholds derived for each grid location using surface water statistics plus parameters related to basin hydrologic characteristics. The flood thresholds are typically at the 95th percentile of the water depth or streamflow values.

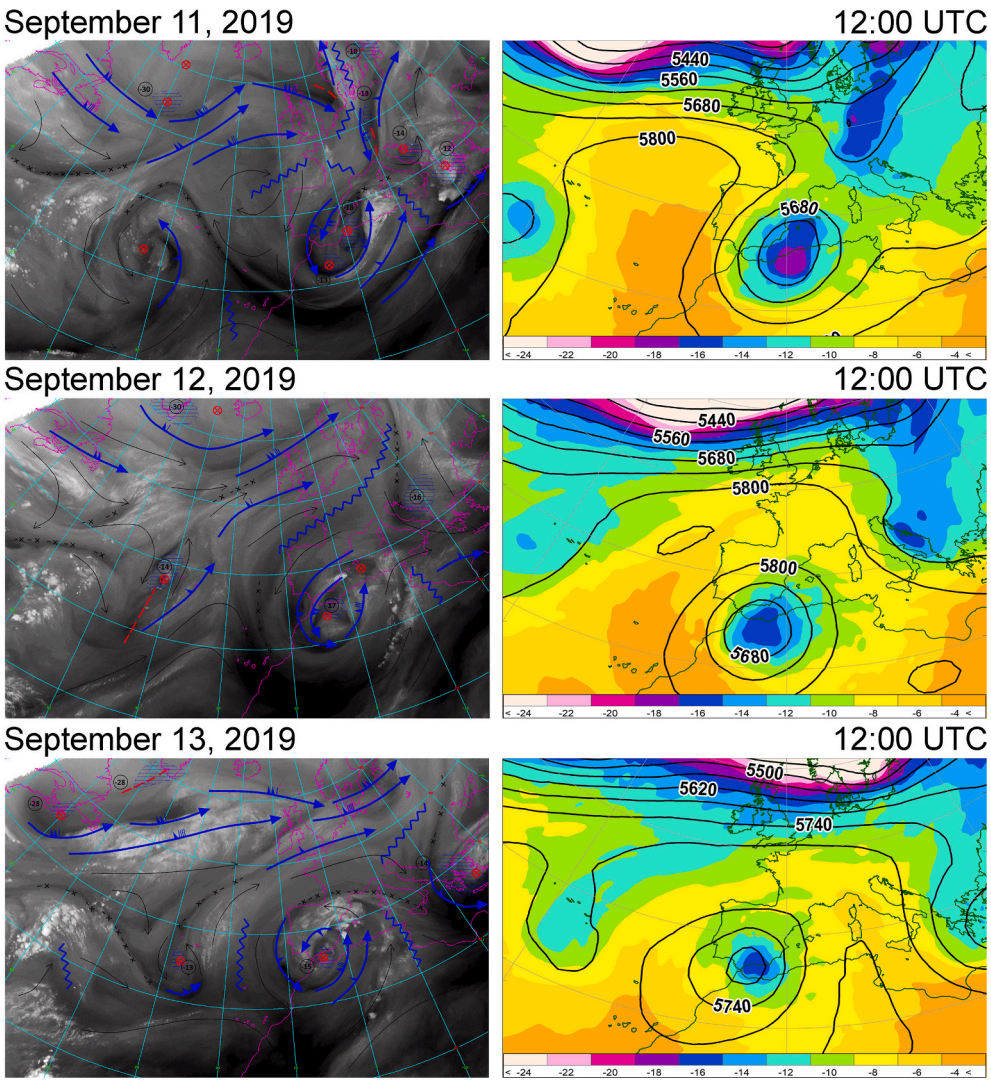

Fig. 3. Diagnostic guides of the event: IR (6.2 μm) satellite imagery with superimposed forecaster diagnostics (left column) and ECMWF's ENS-IFS (0.25°) analyses (geopotential and 500 hPa temperature, right column).

The flood model in the GFMS is based on the University of Washington Variable Infiltration Capacity (VIC) land surface model (Liang et al., 1994, 1996) coupled with a dominant river tracing-based runoff routing model to form the Dominant river tracing-Routing Integrated with VIC Environment (DRIVE) model (Wu et al., 2012, 2014). The GFMS utilizes the DRIVE model to predict hydrological variables over the global domain, including streamflow, flood intensity and inundation (1 km resolution). The global flood system and the DRIVE model have been evaluated based on 15-year (1998–2012) retrospective simulation against more than 1000 gauge streamflow observations and more than 2000 reported flood events across the globe (Wu et al., 2014).

As described in Wu et al., 2014, the surface water storage is the depth [mm] of the surface water above dry ground. At 1/8th degree resolution, the flood intensity value is the calculated water depth [mm] above the flood threshold. Calculations of streamflow [m^3/s] are also shown as well as streamflow values above a flood threshold determined from retrospective model runs at 1/8th degree resolution. The 1 km inundation map at every 3-h time step is derived based on the routing at 1 km resolution and the surface water storage at the same time step by masking out the normal (or referential) water coverage from it. The calculations are for natural systems and do not include the changes in topography caused by man-made constructions.

3. Results and discussion

Model analyses and satellite observations show that on September 9, 2019 a cut-off low detached and isolated from the general circulation at medium and high levels in the North of the British Isles. One of the factors that explains the dropping of this low is the disturbance caused in Newfoundland by Hurricane Dorian as the system moved north downstream over the western flow at medium and high levels of the troposphere.

Fig. 3 shows AEMET's National Prediction Center technical forecasting guides (left) for September 11, 12 and 13, and the geopotential and 500 hPa temperature fields from the HRES-IFS (right). The diagnostic guide is drawn by the forecasters using the IR 6.2 μm data, which provide a day and night picture of the cloud cover and show the higher tops of the clouds. The forecasters identify the low-pressure centers, the thoughts and the fronts using image interpretation techniques. Both sides of Fig. 3 show two different perspectives of the evolution of the low, which developed from a cold (−20 °C) vortex over the Balearics. The ridge off the NW of the Portuguese coast responsible for the blocking is apparent in both the upper-level water vapor imagery and in the ECMWF analyses. The unusually long stationarity of the low (48 h) and the induced, extremely humid westerly flow from a warm Mediterranean, resulted in a low-level atmospheric river that fueled the system

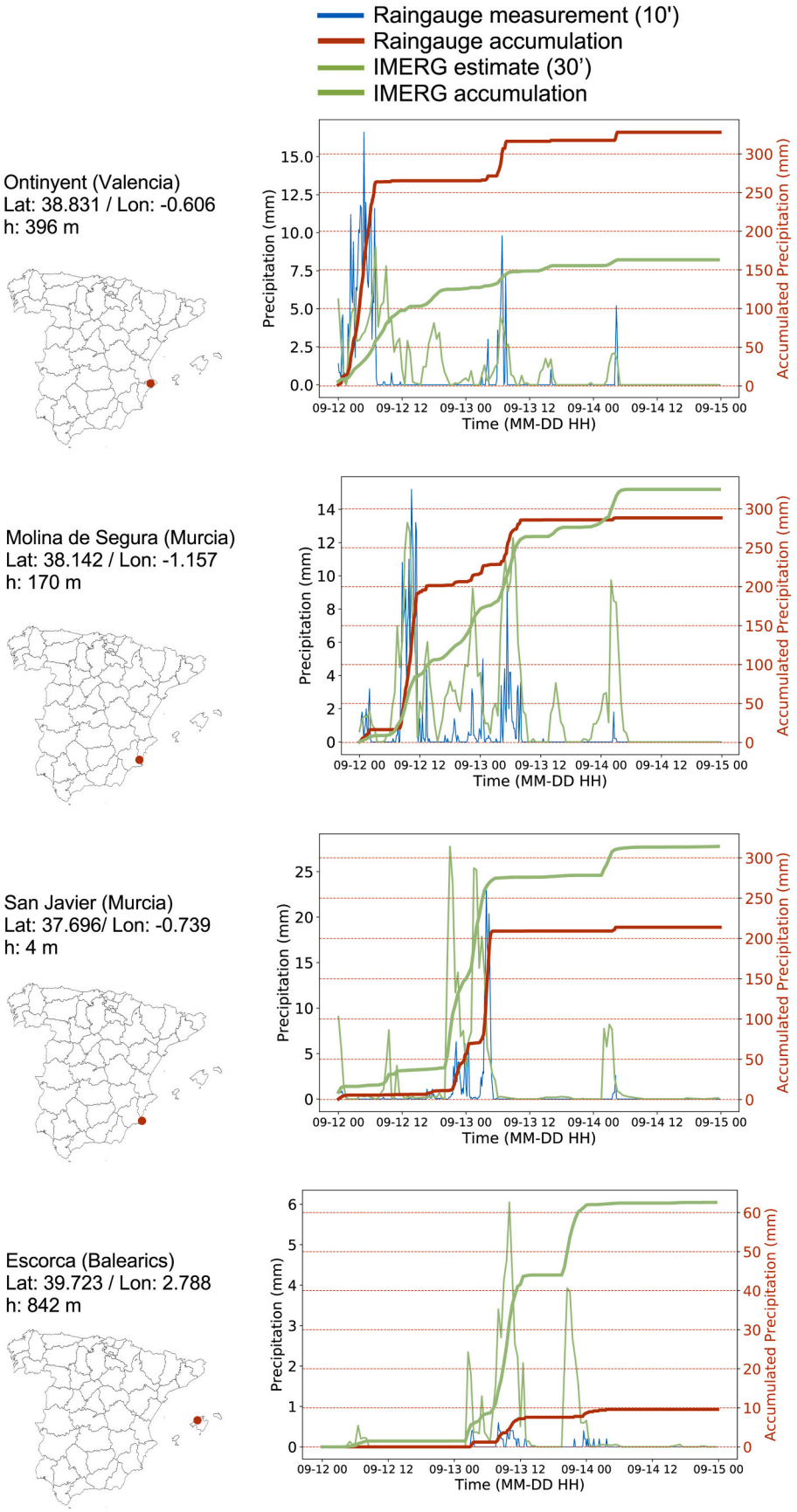

Fig. 4. 10-min pluviographs for four selected stations and 30-min IMERG estimates. Time runs from 00:00 UTC September 12 till September 15, 00:00 UTC.

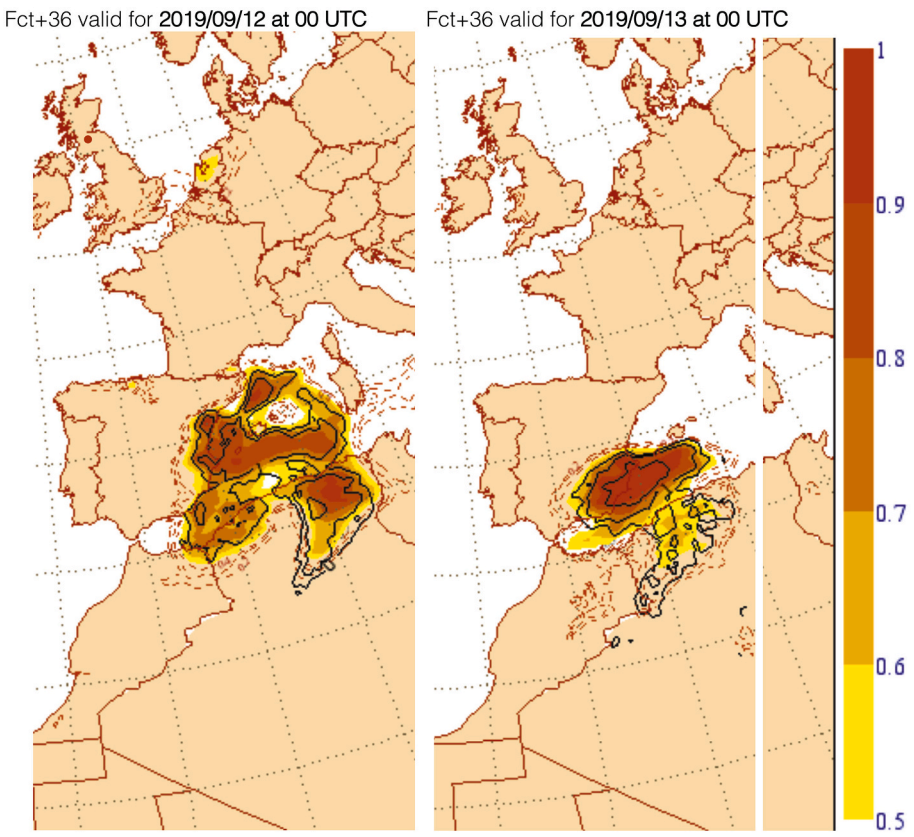

Fig. 5. Extreme Forecast Index (EFI) in the last 24 h (color) and Shift of Tails (SOT, black contours) from the ECMWF ENS-IFS (0.25°). Left: 20190910 at 12 UTC H + 36 forecast, valid for 20,190,912 at 00 UTC. Right: 20190911 at 12 UTC H + 36 forecast, valid for 20,190,913 at 00 UTC.

and yielded the high intensities of precipitation of the episode.

Throughout Tuesday, September 10th, the low advected from north to south through the east of the Iberian Peninsula bringing heavy rainfall to the island of Mallorca. Subsequently, the low continued its advection towards the south, remaining stationary the 12th and the 13th over the southeast of the Peninsula (Fig. 3). This particular location was due to the existence of an extensive blocking dorsal over Western Europe at mid-levels. That prevented the low from moving north and joining the general flow. This blockage contributed to the long persistence and high intensity of precipitation, especially in Murcia and the south of Alicante provinces. These were the areas most affected by the event (Fig. 4).

Four different prediction systems were available to the forecasters in the actual, real-time management of the storm: two regional models for the short range (HARMONIE-AROME and γ-SREPS), and the HRES-IFS and the ENS-IFS ensemble (Molteni et al., 1996) for the medium range. According to these systems the most severe situation was expected in the southeastern areas of the country for Thursday, September 12th. Specifically, southern Valencia province and wide areas of Alicante and Murcia provinces were very likely to endure heavy showers, thunderstorms, and torrential rains (intensities over 60 mm/h for Friday, the 13th). Persistent precipitations (accumulations over 200 mm in 12 h) were also forecasted for the area.

Following the protocol, forecast guidance and early warnings were issued by AEMET's 'Severe Weather Forecasting and Watch National Plan' twin tools, namely 'Meteoalerta' and 'Meteoalarm' (EUMETNET, 2006). Meteoalarm was built for the purpose of providing the most relevant information needed to prepare for extreme weather and operates within the Meteoalarm European framework (www.meteoalarm.eu). Given the critical severity of the forecasts and according to Meteoalarm rules, special warning reports were issued from Sept 9th and updated regularly up till Sept. 12th. They contained a description of the phenomenon and estimates of timing and probability (which was above 80% i.e. very high), as well as an indication of the severe weather events expected to occur at the surface.

Early warning maps were regularly updated at the AEMET website (www.aemet.es) on September 11th, 12th and 13th. For several areas of Valencia, Alicante and Murcia, the first orange warning was issued on Sept. 9th at 2150 UTC (valid for September 12th) for 40 mm/h accumulation and 100 mm/12 h. The first red warning was issued on Sept. 11th at 0929 UTC (valid for September 12th) for 90 mm/h (70 mm for Murcia) and 180 mm/12 h (200 mm for Murcia). A number of additional orange and red warnings were updated on September 9–12 for the 12th–13th.

The episode was correctly forecasted by the EFI. Fig. 5 shows September 12 (left) and 13 (right) forecasts for the next 36 h. The most damaged areas were precisely identified, with EFI values greater than 0.9. Fig. 6 shows that the 'Point Rainfall' product was also precise. The results depict the cumulative Distribution Functions (CDF) for the latest 10 passes of the ENS-IFS model for 24 h accumulations over the city of Murcia (pinpointed in the map) for day 12. The x-axis (Fig. 6, bottom) is for the precipitation values while the y-axis indicates the probability of the forecast being below that value. The red line indicates the final pass. The median is close to 100 mm/24 h. The increase in the slope of the curve is indicative of increased reliability over previous passes and denotes highly predictability. The ensemble is made of 50 + 1 members, thus encompassing a large uncertainty in the predicted accumulated precipitation.

Fig. 7 compares the IMERG ("Early") instantaneous satellite estimates (right) at four key moments of the event with the corresponding ground radar images (left). The agreement is noticeable in the location of the precipitation. Regarding intensity, only a qualitative assessment can be made as the national radar network uses a fixed Marshall and Palmer Z/R relationship that precludes a more detailed comparison. The actual relationship is $Z = 200R^{1.6}$, where Z ($mm^6\ m^{-3}$) is the reflectivity

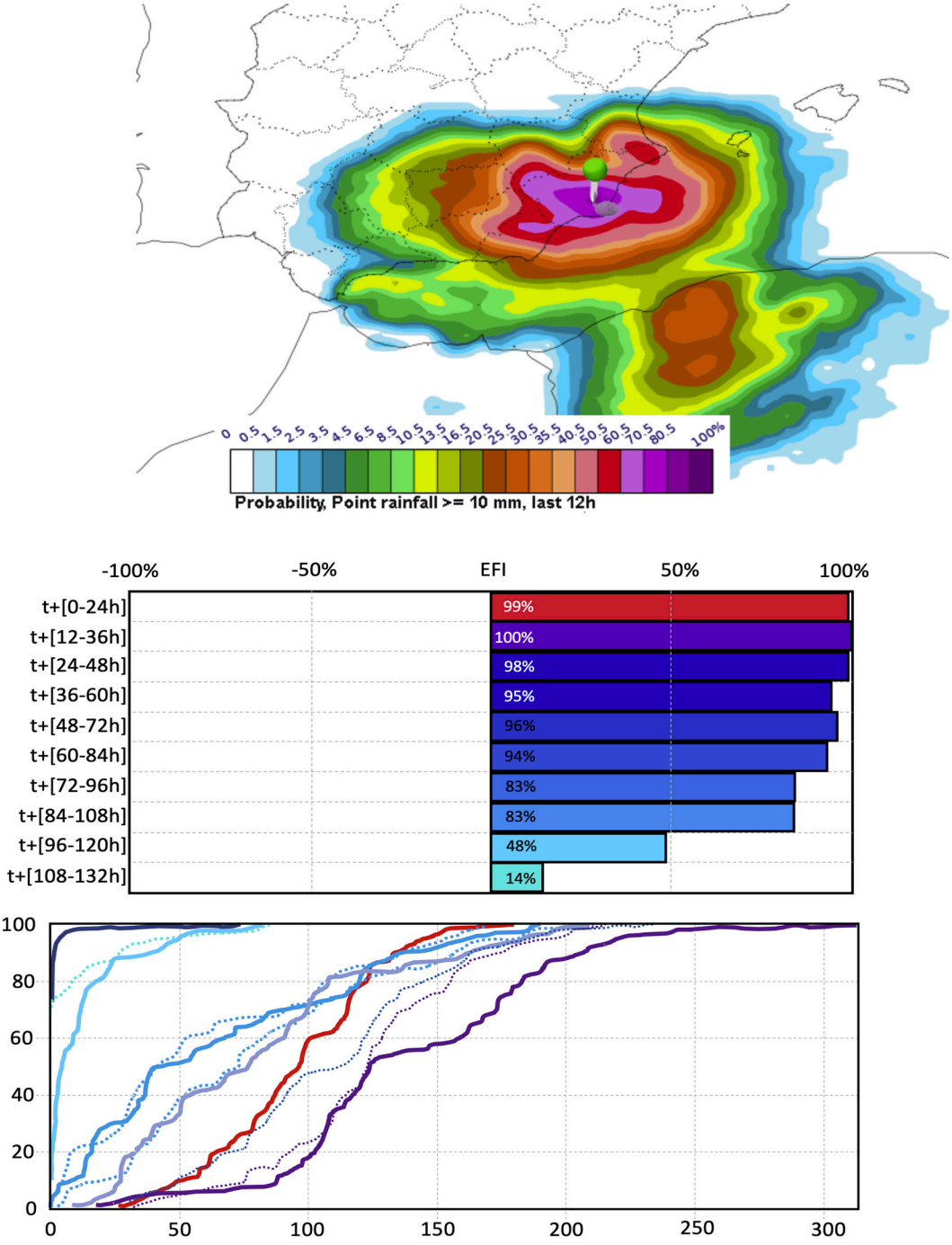

Fig. 6. (top) ECMWF's Point Rainfall probability for 12 h precipitation exceeding 10 mm in Murcia city for the period September 12, 18 UTC to September 13, 06 UTC (middle) Extreme forecast index (EFI) for 24 h total precipitation (mm) in Murcia city. Base date: Sep 12, 00 UTC. Valid for +24 h, from Sep 12, 01 UTC to Sep 13 at 00 UTC. (bottom) Corresponding ENS cumulative distribution function (CDF). The latest value is the red line.

factor and R (mm/h) is the rainfall rate. The coefficient and the exponent are representative of stratiform precipitation, which is certainly not the case here.

Fig. 8 illustrates the evolution of the episode using the IMERG. The fine spatial resolution and the frequency of the estimates is especially useful outside the radar coverage as the storm developed over the Mediterranean. The 30 min estimates are also useful to assist the forecasters in operations, giving more or less credibility to the several model outputs and thus guiding the nowcasting.

The quantitative evaluation for accumulated values as provided by the satellites can be assessed by comparing with AEMET's rain gauge analyses (Fig. 9, right). The IMERG accumulations (Fig. 9, middle) are consistent in pattern considering the interpolation effects in the fields due to the sparseness of the ground network. Overall, the satellite estimate identifies the areas of maximum precipitation, and shows a good visual agreement with the pattern of the surface observations. This is consistent with previous findings: the daily correlation of the IMERG Final estimates (the best IMERG product, produced about 3 months after the satellite data is first available) and AEMET observations over Spain (March 2014 to May 2017) is $R^2 = 0.77$, with little bias (Fig. 11, linear regression line for daily data: AEMET = 1.062*IMERG-0.137, Tapiador et al., 2020; for TMPA the correlation is 0.79 R^2 and the regression

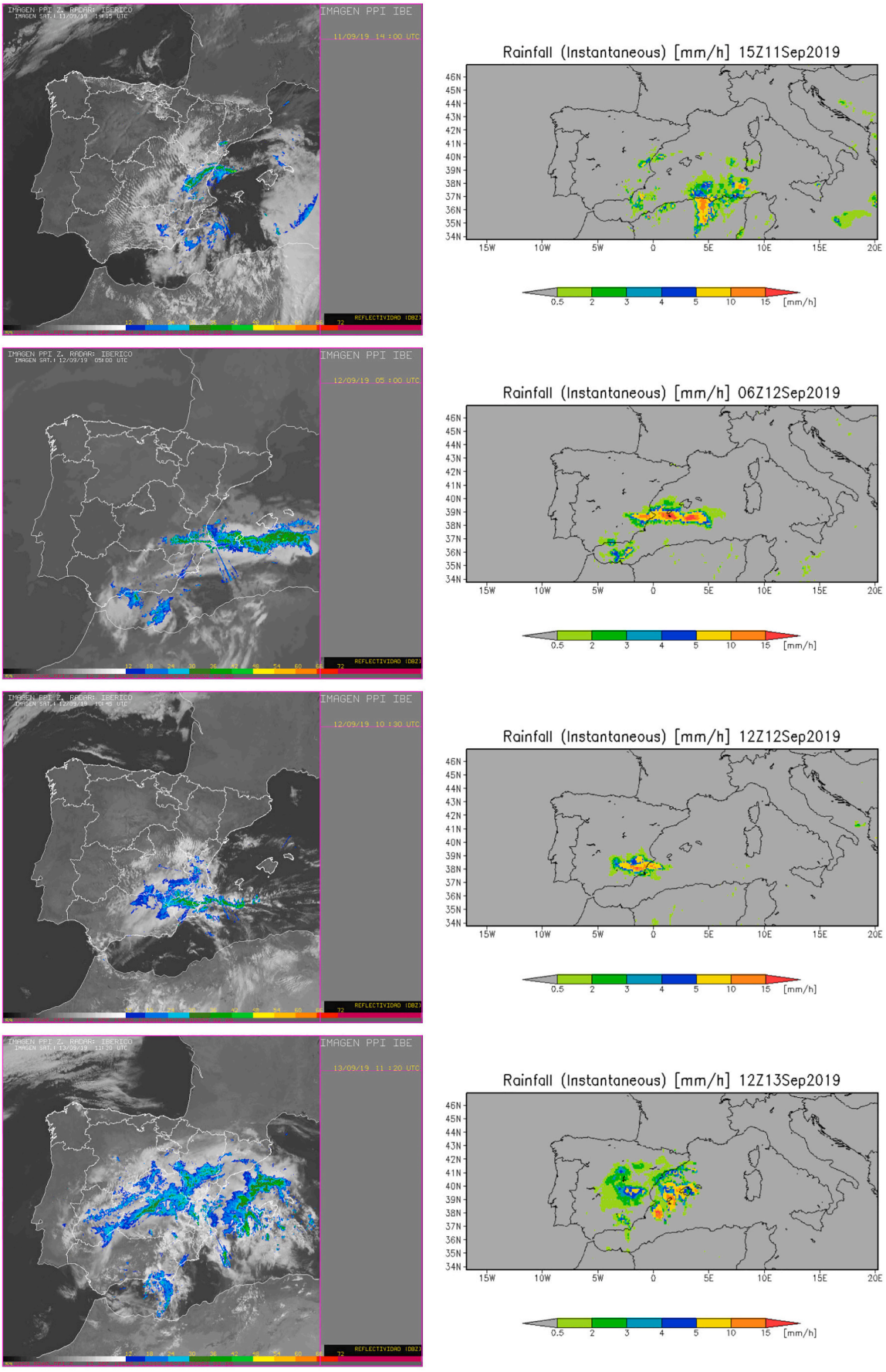

Fig. 7. Ground radar estimates of rainfall (left) and satellite estimates (right) for four selected times in the episode.

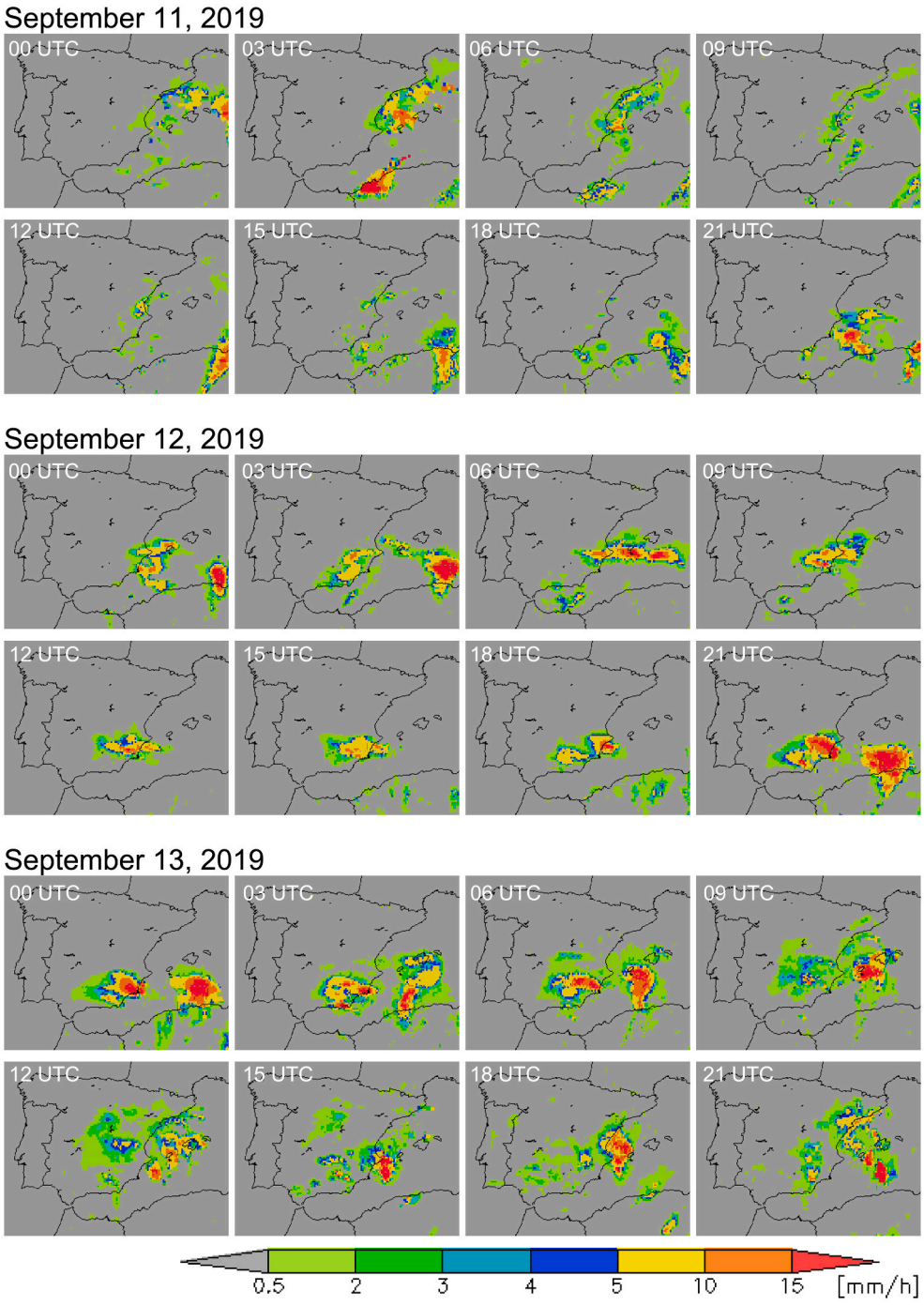

Fig. 8. Instantaneous precipitation estimates from the GPM satellites (IMERG-E product) every 3 h.

AEMET = 1.089*TMPA-0.188). However, the IMERG Final product includes monthly surface gauge information that aids in reducing the bias. Indeed, the correlations between the IMERG-Final estimates and rain gauges depend only on the performances of the IMERG regression method: for the actual location of the rain gauges they should be the same. On contrast, the IMERG-Early product uses only satellite information. Therefore, the performances of IMERG-Early are intrinsically worse than for IMERG-Final, as shown below. However, this is the product that could be used for real-time monitoring and real-time hydrological calculations.

As has already been seen in Fig. 4, the IMERG estimates catch the individual rain events, but the estimates vary from case to case, with some higher and some lower in terms of final accumulation. Matching individual gauges with the 0.1 degree latitude-longitude IMERG grid at 30-min. Intervals provides a high degree of uncertainty. Using a daily total and many stations helps to define the quantitative relation between the IMERG-Early estimates and the AEMET observations. Fig. 10 shows these results for the three key days of this flooding event. Despite the time accumulation up to a day there is still a very large scatter. A number of AEMET stations have daily totals of over 150 mm. IMERG has even more matched points with values over that value, although most of such points are not co-located with the large gauge values. This variability is not surprising considering the spatial variance of convective rainfall. As can be seen from the daily plots, in general IMERG is providing an

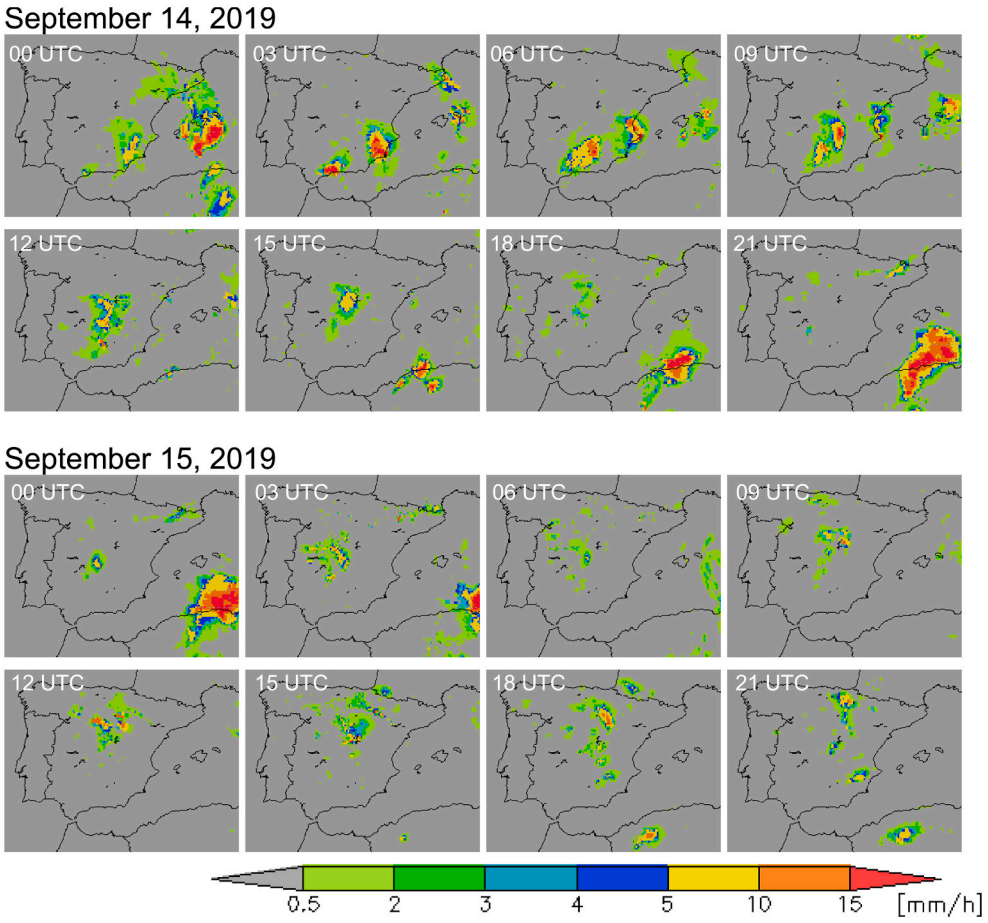

Fig. 8. (*continued*).

overestimate of values compared to the gauge measurements. This overestimate tendency is noticeable even near origin with relative light rainfall amounts (e.g., < 20 mm in AEMET). Overestimates are also evident at higher amounts. Combining all three days, the overall bias (E[IMERG]-E[AEMET]) for IMERG is 5.71 mm, with a bias ratio (E[IMERG]/E[AEMET]) of 2.06. This analysis is for one case and additional validation for additional intense rain events is necessary, but it is clear that there is room for improvement in the algorithm.

The usefulness of the high spatial resolution estimates over both land and sea is also exemplified by inspection of the 0.5° Climate Prediction Center (CPC) gauge analysis (Fig. 9, left). Despite the fact that the precipitation patterns are identified, the limited number of rain gauges used by this product and the coarse resolution is clearly insufficient to be compared with IMERG and AEMET rain gauges. Fig. 11 illustrates this point for the area of interest. The required interpolation for grids without CPC gauges makes the precipitation field artificially smooth to ascertain how well IMERG represents the actual precipitation, which is better featured by AEMET denser network.

Overall, the IMERG compares well with the pattern of the observations for this particular extreme hydrometeorological event, but with a considerable overestimation. This still confirms the usefulness of an IMERG-type product for nowcasting, considering the demanding spatial and temporal resolution required. There is an instance, however, in which IMERG and ground data appear to differ in and that is in the city of Orihuela (Fig. 12). This case is interesting as it shows one of the issues affecting satellite precipitation estimates. Expert analysis by AEMET meteorologists indicate that fast dynamics and deep convection produced noticeable wind gusts and large hail that feature conspicuously in radar images. However, precipitation lasted just 10 min over Orihuela station and produced only moderate accumulations. A direct translation of those radar reflectivities into precipitation severely overestimates the total precipitation, artificially converting high reflectivities into high rainfall rates. Comparison of the accumulated totals for the high-quality, 10-min gauge data for this location and the stations featured in Fig. 4, and careful examination of the records of the station indicate that the rain gauge is correct. Both ground radar and the IMERG overestimated the amount, resulting in the conspicuous peak of Fig. 12 (bottom) at 03 UTC September 14th, where a noticeable discrepancy is visible. Overall at this station IMERG final and the gauge estimates are very close at the end of the event. Another interesting disagreement is Escorca station in the Balearics (Fig. 4, bottom row). In this case, the difference is attributable to local topographic effects as the station is located in a narrow valley surrounded by highly contrasted terrain.

Streamflow, streamflow above flood threshold and flood detection/intensity estimates from the GFMS (Fig. 13) are consistent with the observed effects of the episode (Fig. 2) and helps identifying which areas have been more affected by the storm. Indeed, the highest values in the flood detection/intensity plot correspond with the most affected areas (Figs. 1 and 2). IMERG rainfall estimates are the primary input to the GFMS hydrological calculations and the apparent overestimation as compared to gauges should produce overestimates in streamflow and flood parameters. However, the location and clear significance of the event are obvious in the calculations, especially in locations with sparse coverage of raingauges, radar, or streamgauges.

Extreme precipitation events in semi-arid areas of the planet such as southeastern Spain are expected to become more frequent under increasing global warming conditions. These projections, however, do not always translate directly into infrastructure decisions. Fig. 14 depicts the official flood risk areas delineated by the Ministry for the Ecological Transition. In spite of the known risks (cf. Valenzuela et al.,

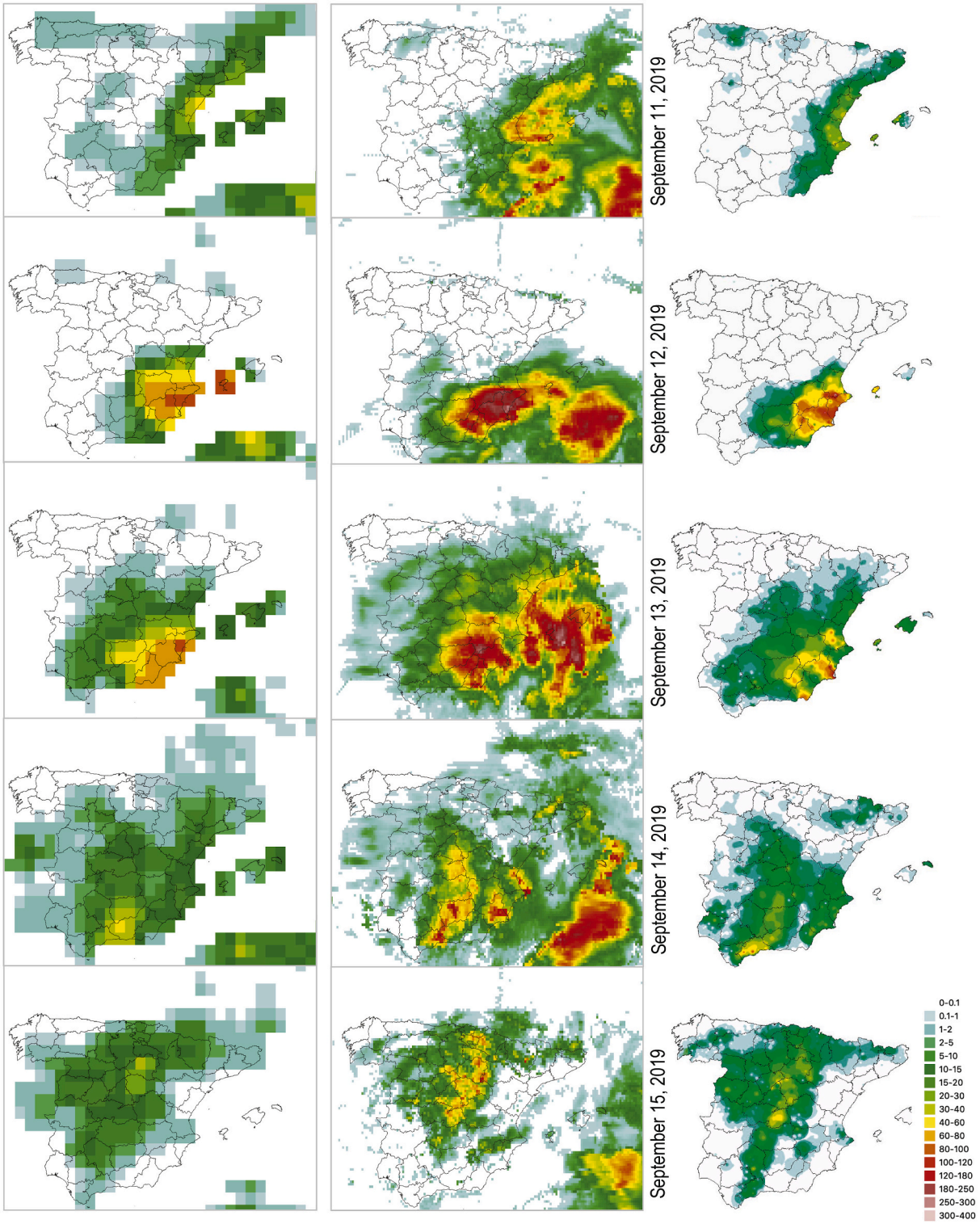

Fig. 9. Daily accumulations (mm) for CPC rain gauges (left), the GPM satellites estimates (IMERG, middle) and AEMET's rain gauges. Units are mm/day.

2018), human constructions have traditionally occupied the riverbeds and riverbanks, most of which are today heavily urbanized. The structure of the settlements, and not only increased frequency or intensity of precipitation, is a major risk factor and the main cause of casualties and damages. Early alerts and forecasts can help palliating the losses, but intelligent planning and law enforcement would be more effective to minimize the mounting costs of severe weather in the Mediterranean. The reasons behind people building in flood risk areas are complex and include irrational behavior, necessity and opportunism, so a comprehensive and intelligent approach in required to enforce sustainable development in such areas.

4. Conclusions

In nowcasting operations, it is really important to look at the data to evaluate if the models are forecasting correctly. Even in the cases the

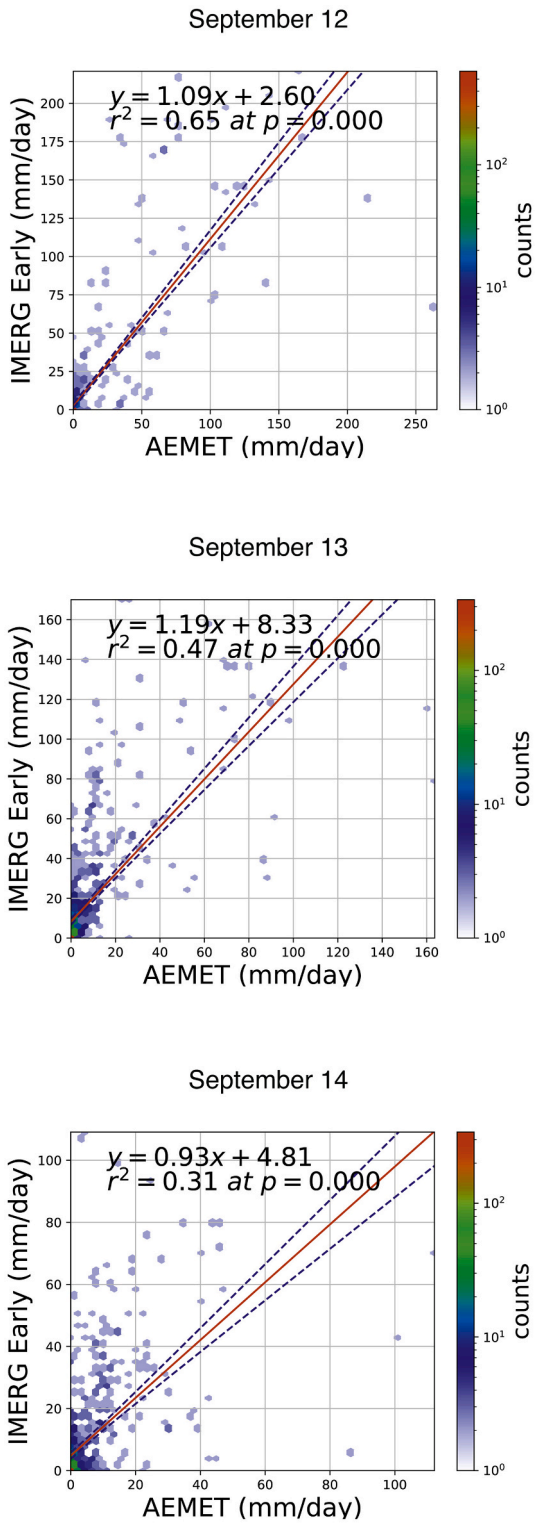

Fig. 10. Comparison of the daily IMERG Early estimates and the accumulated values for each one of the 706 automatic, 10 min sampling stations from AEMET. The *p*-value is a two-sided p-value of Pearson correlation coefficient *r* and indicates the probability of an uncorrelated system producing data that have a Pearson correlation at least as extreme as the one computed from these datasets (i.e. negligible in these cases).

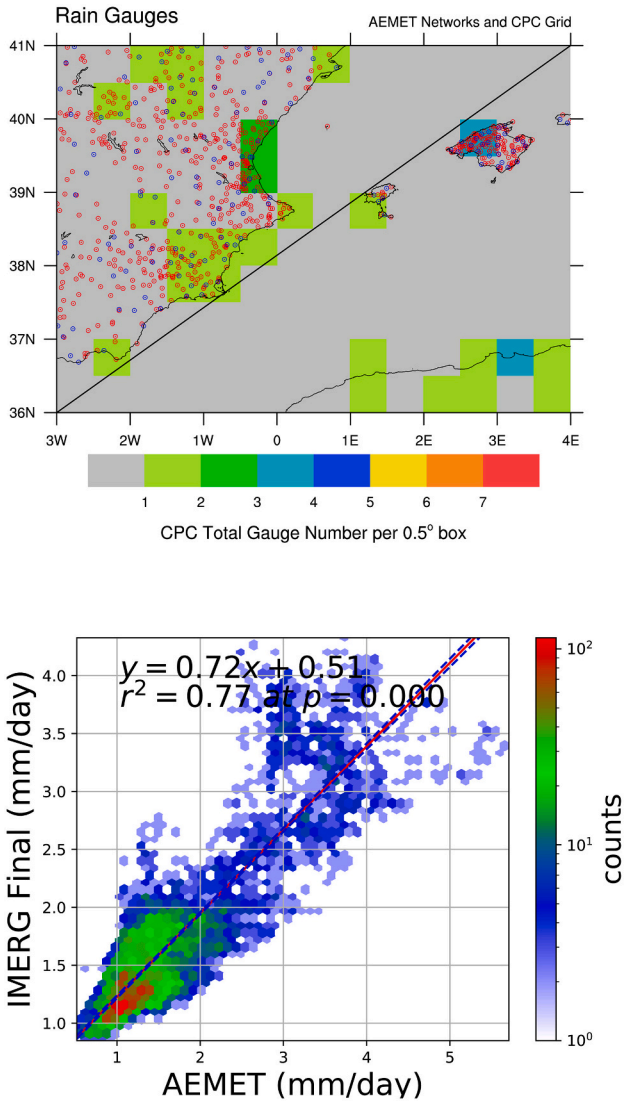

Fig. 11. (top) Rain gauge distribution for the area of interest and (bottom) scatterplot of the daily IMERG estimates and AEMET observations for the period March 2014 to May 2017 over the whole country (from Tapiador et al., 2020).

models are very good such as the one presented here forecasters need to validate with actual events. Here, it has been shown that the IMERG early product can provide a correct indication of the major features of the event, including precipitation patterns.

Indeed, satellite data are increasingly useful for the analysis of extreme hydrometeorological events (Levizzani and Cattani, 2019; Michaelides, 2013, 2019). Since 2014, the GPM constellation has been providing more detailed and frequent estimates of precipitation. Integration of these into even simple hydrological models produces estimates of streamflow and flood intensity that are useful not only for rapid response but also for planning.

The IMERG compares well with observations in general for the major 2019 September floods in Spain. This is true especially in terms of pattern and timing, although the IMERG-Early (satellite data only) appears to overestimate the rainfall for this event. More general validation of IMERG and similar products, especially for intense rain events should be a focus for the future to understand the variability and limitations of satellite-based precipitation estimation techniques and to point the way for improvements. Another major issue which is observed in this case is the misinterpretation of localized and short duration high reflectivities

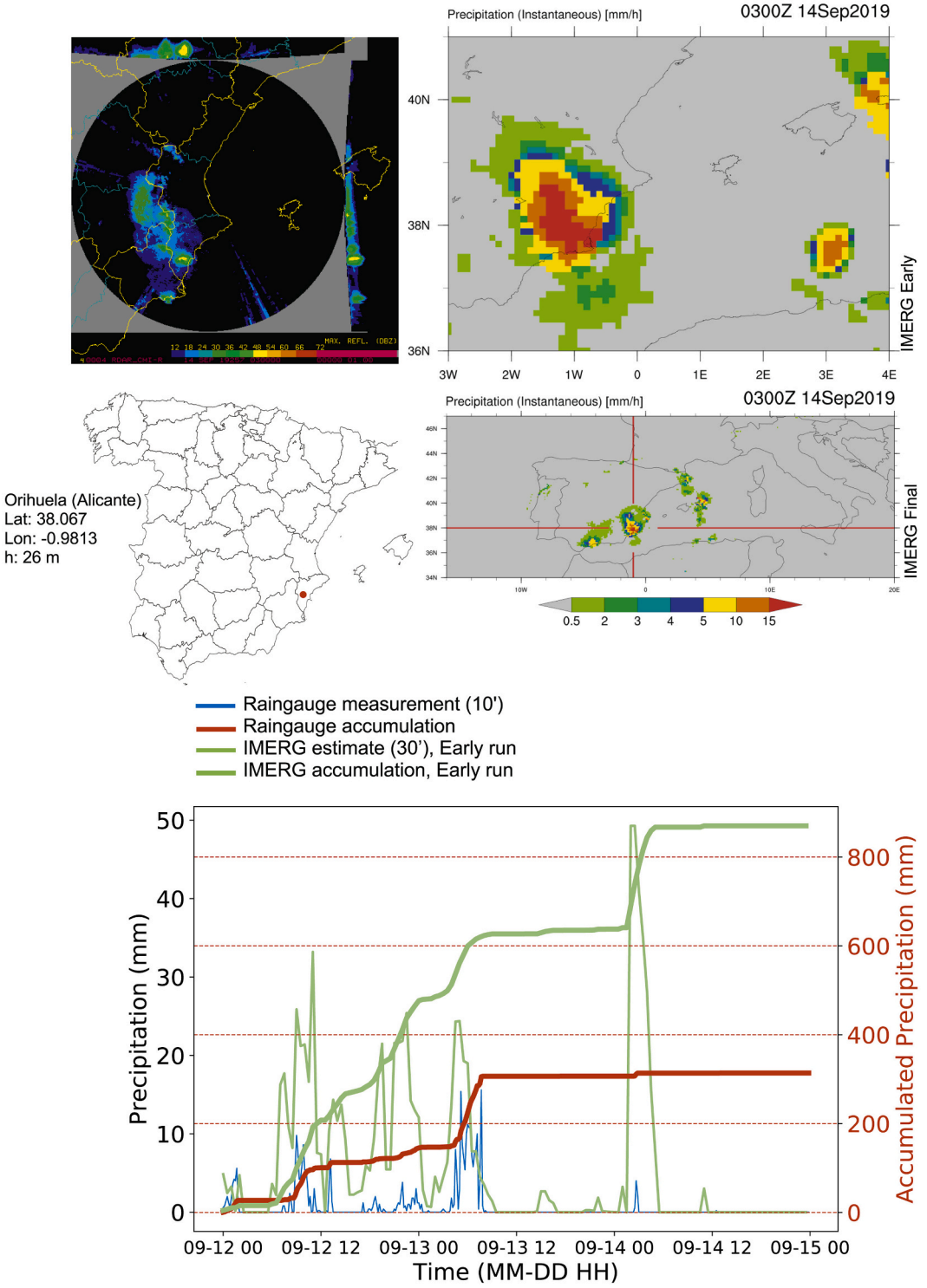

Fig. 12. (top) Instantaneous ground radar (top, left) and GPM (top, right) estimates for September 14 at 03:00 UTC over Orihuela. (bottom) Time series of 10 min rainfall, 30 min IMERG estimate and accumulated precipitation as measured by the Orihuela station (Lon: −0.944, Lat: 38.084) and the IMERG, from September 12, 00:00 to September 15, 00:00.

due to hail that are propagated by the algorithm and result in too much rain over extended areas. More research on the effects of deep convection over land would certainly improve the capabilities of the constellation in severe weather. Mismatches in mountain areas also feature in this study case, highlighting the importance of orography in precipitation research and the difficulties of precisely determining by satellite the exact amount of rainfall in narrow valleys.

Our study focuses on a single event so no general conclusions can be drawn on the overall utility of satellite data for analyzing extreme events. For our case, however, the GFMS provides an accurate picture of the evolution of the event. While the GFMS was not directly used for the management of the storm in this case, the results are coherent enough to state that the GFMS can be a useful tool for rapid response to floods in many countries, especially where conventional coverage is lacking.

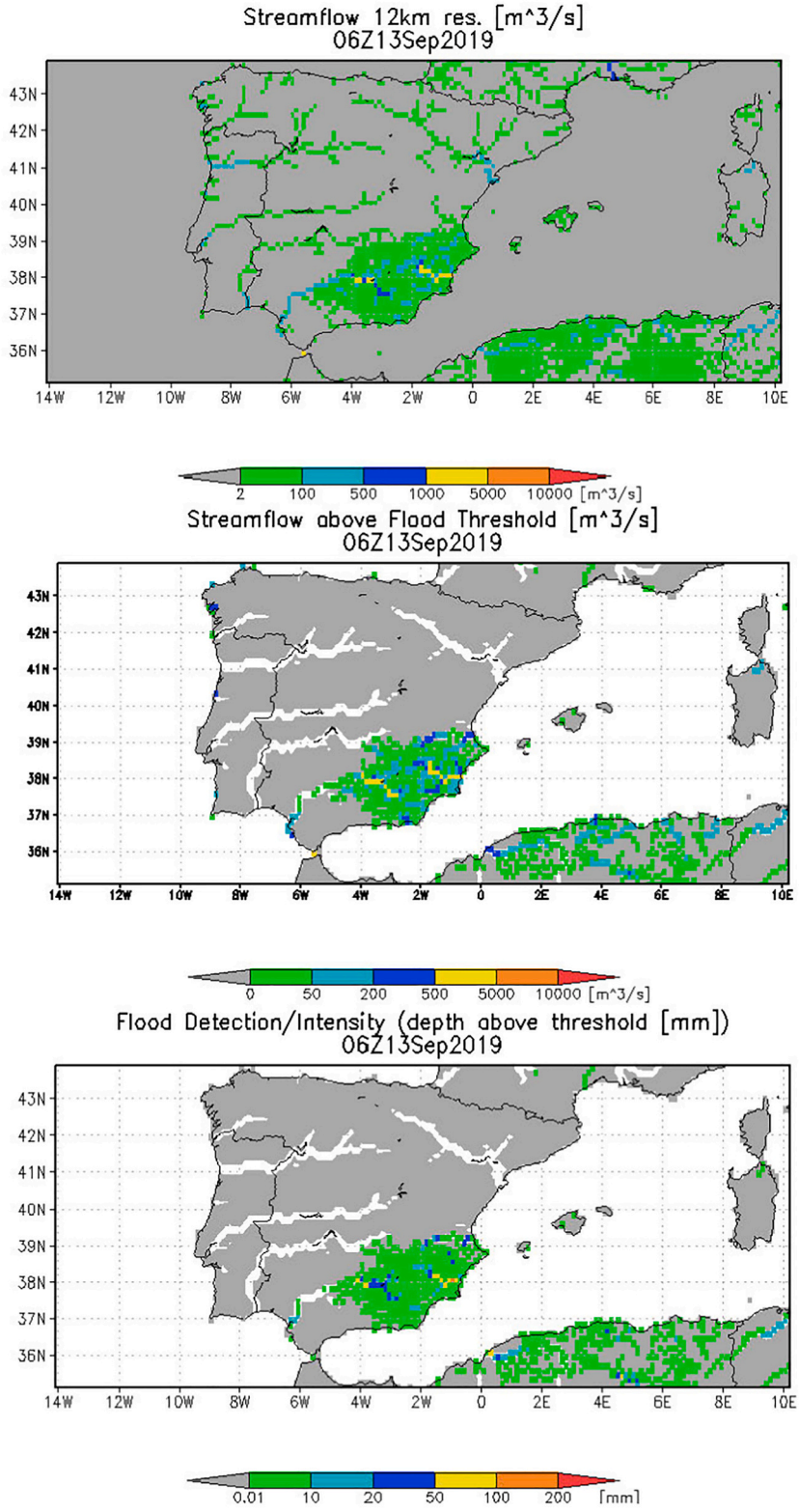

Fig. 13. Stream flow at 12 km resolution (top), streamflow above flood threshold (middle), and flood detection/intensity (bottom) for 5:00–6:00 UTC, September 13.

Regarding the use of satellite data, the GPM Core Observatory with the directness of the DPR provides possibilities to improve the estimated rain that goes into the hydrological model and provide more accurate flood information.

To conclude, it seems that the integration of satellite estimates with numerical forecasts is unavoidable. At the end, a major goal is to be able not only to observe but to predict severe hydrometeorological episodes. While completely automated (unassisted nowcasting techniques) are still in development forecasts from NWP models are becoming consistent enough to permit to launch alerts well in advance. The current limitations in terms of timing and precise location of the extreme precipitation events, and the fear to false alarms should not preclude communicating

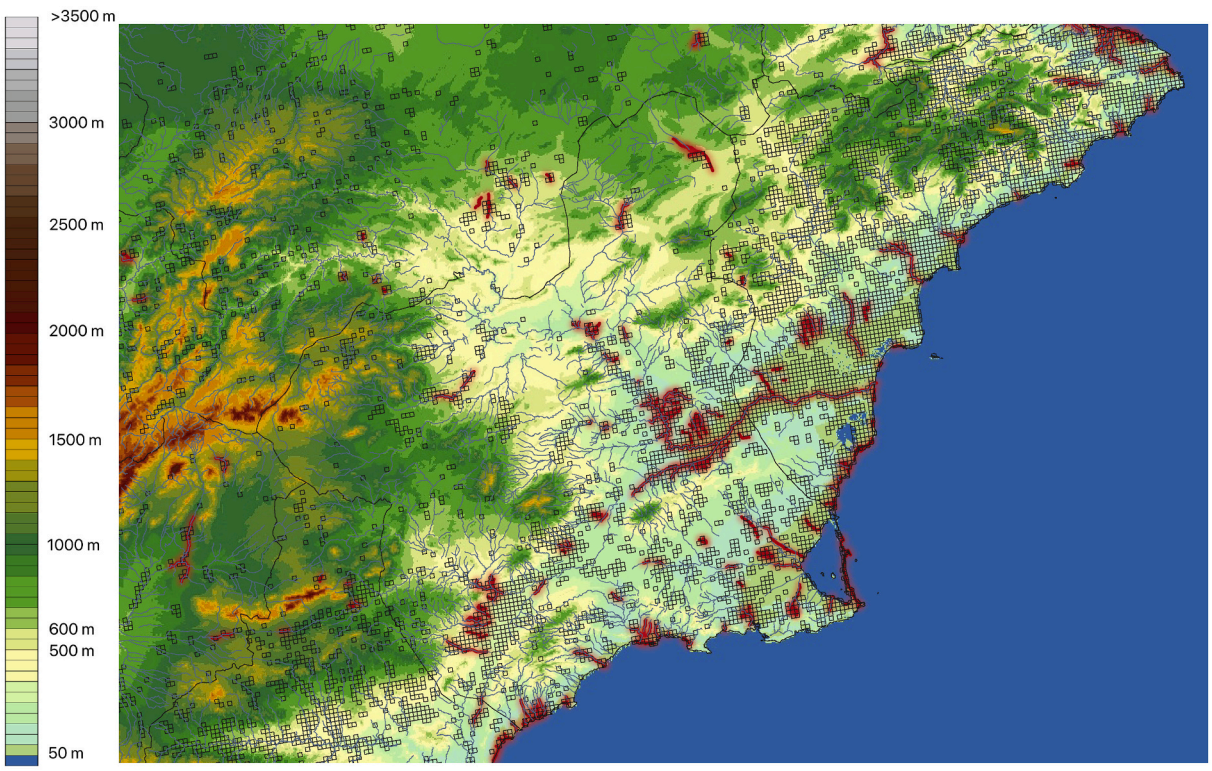

Fig. 14. Major rivers, flood risk areas (red neon, Ministry for the Ecological Transition, MITECO, 2018) and human constructions (tilted squares, National Institute for Statistics INE, 2018) over the topography map.

the risks to decision makers so such information is used in operations. Guidance by satellite products such as IMERG can assist in a task of clear societal interest.

Indeed, short-term predictions based on satellite data are fundamental for societal readiness on these extreme events, but the role of nowcasting and expert judgment is still critical. The interpretation of dissimilar and sometimes conflicting data (such as ensemble member outliers, or anomalous reflectivities) depends on a judicious choice based on experience and familiarity with the dynamics of the area. With new advances in nowcasting coming from artificial intelligence techniques more automated procedures can be envisioned. Improvement in model resolution will certainly help. As we approach the 'model singularity', i.e. the point in which models will catch up with observations in terms of spatial and temporal resolution, accuracy and precision, less and less human interaction and subjective evaluation will be required. However, expert judgment in severe weather episodes risking life and property is unlikely to be replaced by algorithms in the near future. The task of issuing warnings and alerts is a delicate mix of sometimes conflicting and blurry requirements, and at the end tanking action involves both policy decisions and accountability.

Data availability statement

GFMS data can be accessed at http://flood.umd.edu/. GPM data and products are openly available through https://gpm1.gesdisc.eosdis.nasa.gov. Because of the proprietary nature of the AEMET data used in this study, access is restricted. Contact cmarcosm@aemet.es for complete access and usage information.

Declaration of Competing Interest

The authors declare that they have no known competing financial interests or personal relationships that could have appeared to influence the work reported in this paper.

Acknowledgements

Funding from projects PID2019-108470RB-C21, PID2019-108470RB-C22 (AEI/FEDER, UE), CGL2016-80609-R, and 1365002970/KMA2018-00721 (Korean Meteorological Agency, Korea) is gratefully acknowledged.

References

Anagnostou, E.N., 2010. Remote sensing for precipitation and hydrologic applications. In: Advances in Data-based Approaches for Hydrologic Modeling and Forecasting, pp. 245–266.

Asong, Z.E., Razavi, S., Wheater, H.S., Wong, J.S., 2017. Evaluation of Integrated Multisatellite Retrievals for GPM (IMERG) over Southern Canada against Ground Precipitation Observations: a preliminary Assessment. J. Hydrometeorol. 18, 1033–1050. https://doi.org/10.1175/JHM-D-16-0187.1.

Belabid, N., Zhao, F., Brocca, L., Huang, Y., Tan, Y., 2019. Near-real-time flood forecasting based on satellite precipitation products. Remote Sens. 11. https://doi.org/10.3390/rs11030252.

Bengtsson, L., et al., 2017. The HARMONIE–AROME model configuration in the ALADIN–HIRLAM NWP system. Mon. Weather Rev. 145 (5), 1919–1935. https://doi.org/10.1175/MWR-D-16-0417.1.

Berthou, S., Mailler, S., Drobinski, P., Arsouze, T., Bastin, S., Béranger, K., Lebeaupin Brossier, C., 2018. Lagged effects of the Mistral wind on heavy precipitation through ocean-atmosphere coupling in the region of Valencia (Spain). Clim. Dyn. 51 (3), 969–983.

Bougeault, P., Mascart, P., 2009. The Meso-NH atmospheric simulation system: scientific documentation part III: physics. Tech. Rep. (no doi), URL: http://mesonh.aero.obsmip.fr/mesonh/dirdoc/book1m4819jan2009/scidocp3.pdf.

Cattani, E., Torricella, F., Laviola, S., Levizzani, V., 2009. On the statistical relationship between cloud optical and microphysical characteristics and rainfall intensity for convective storms over the Mediterranean. Nat. Hazards Earth Syst. Sci. 9, 2135–2142. https://doi.org/10.5194/nhess-9-2135-2009.

Champagne, C., Davidson, A., Cherneski, P., L'Heureux, J., Hadwen, T., 2014. Monitoring agricultural risk in Canada using L-Band passive microwave soil moisture from SMOS. J. Hydrometeorol. 16, 5–18. https://doi.org/10.1175/JHM-D-14-0039.1.

Cortès, M., Llasat, M.C., Gilabert, J., Llasat-Botija, M., Turco, M., Marcos, R., Martín Vide, J.P., Falcón, L., 2018. Towards a better understanding of the evolution of the flood risk in Mediterranean urban areas: the case of Barcelona. Nat. Hazards 93, 39–60. https://doi.org/10.1007/s11069-017-3014-0.

Cortès, M., Turco, M., Ward, P., Sánchez-Espigares, J.A., Alfieri, L., Carmen Llasat, M., 2019. Changes in flood damage with global warming on the eastern coast of Spain. Nat. Hazards Earth Syst. Sci. 19, 2855–2877. https://doi.org/10.5194/nhess-19-2855-2019.

De Coning, E., 2013. Optimizing satellite-based precipitation estimation for nowcasting of rainfall and flash flood events over the south African domain. Remote Sens. 5, 5702–5724. https://doi.org/10.3390/rs5115702.

Dezfuli, A.K., Ichoku, C.M., Huffman, G.J., Mohr, K.I., Selker, J.S., van de Giesen, N., Hochreutener, R., Annor, F.O., 2017. Validation of IMERG precipitation in Africa. J. Hydrometeorol. 18, 2817–2825. https://doi.org/10.1175/JHM-D-17-0139.1.

Di Paola, F., Ricciardelli, E., Cimini, D., Romano, F., Viggiano, M., Cuomo, V., 2014. Analysis of Catania flash flood case study by using combined microwave and infrared technique. J. Hydrometeorol. 15, 1989–1998. https://doi.org/10.1175/JHM-D-13-092.1.

EUMETNET, 2006. Meteoalarm - Severe Weather Warnings for Europe – Main Page. URL: https://www.meteoalarm.eu/ (last visited 2019-10-05).

Frogner, I., Andrae, U., Bojarova, J., Callado, A., Escribà, P., Feddersen, H., Hally, A., Kauhanen, J., Randriamampianina, R., Singleton, A., Smet, G., van der Veen, S., Vignes, O., 2019. HarmonEPS—The HARMONIE ensemble prediction system. Wea. Forecasting 34, 1909–1937. https://doi.org/10.1175/WAF-D-19-0030.1.

Gaona, M.F.R., Overeem, A., Leijnse, H., Uijlenhoet, R., 2016. First-year evaluation of GPM rainfall over the Netherlands: IMERG Day 1 final run (V03D). J. Hydrometeorol. 17, 2799–2814.

Huffman, G.J., Bolvin, D., Nelkin, E.J., 2018a. Integrated Multi-satellitE Retrievals for GPM (IMERG) Technical Documentation. Nasa Technical Documentation, p. 54.

Huffman, G.J., Bolvin, D., Braithwaite, D., Hsu, K.-L., Joyce, R., Kidd, C., Nelkin, E., Sorooshian, S., Tan, J., Xie, P., 2018b. Integrated multi-satellitE Retrievals for GPM (IMERG) technical documentation. In: Algorithm Theoretical Basis Document version 5.2. NASA/GSFC, Greenbelt, MD.

Jakob, C., et al., 2000. The IFS cycle CY21R4 made operational in October 1999. ECMWF Newsletter 87, 2–9.

Kirschbaum, D., Stanley, T., 2018. Satellite-based assessment of rainfall-triggered landslide hazard for situational awareness. Earth's Future 6, 505–523. https://doi.org/10.1002/2017EF000715.

Kolios, S., Feidas, H., 2013. An automated nowcasting system of mesoscale convective systems for the Mediterranean basin using Meteosat imagery. Part I: System description. Meteorol. Appl. 20, 287–295. https://doi.org/10.1002/met.1282.

Lalaurette, F., 2003a. Early detection of abnormal weather conditions using a probabilistic extreme forecast index. Q. J. R. Meteorol. Soc. 129, 3037–3057.

Lalaurette, F., 2003b. Two Proposals to Enhance the EFI Response Near the Tails of the Climate Distribution. ECMWF, pp. 1–8. http://www.ecmwf.int/products/forecasts/efi-guide.pdf.

Lascaux, F., Richard, E., Pinty, J.-P., 2006. Numerical simulations of three different MAP IOPs and the associated microphysical processes. Q. J. R. Meteorol. Soc. 132 (619), 1907–1926. https://doi.org/10.1256/qj.05.197.

Laviola, S., Moscatello, A., Miglietta, M.M., Cattani, E., Levizzani, V., 2011. Satellite and Numerical Model Investigation of two Heavy rain events over the Central Mediterranean. J. Hydrometeorol. 12, 634–649. https://doi.org/10.1175/2011JHM1257.1.

Levizzani, V., Cattani, E., 2019. Satellite Remote Sensing of Precipitation and the Terrestrial Water Cycle in a changing climate. Remote Sens. 11, 2301. https://doi.org/10.3390/rs11192301.

Liang, X., Lettenmaier, D.P., Wood, E.F., Burges, S.J., 1994. A simple hydrologically based model of land surface water and energy fluxes for GSMs. J. Geophys. Res. 99 (D7), 14,415–14,428.

Liang, X., Wood, E.F., Lettenmaier, D.P., 1996. Surface soil moisture parameterization of the VIC-2L model: Evaluation and modification. Glob. Planet. Chang. 13, 195–206. https://doi.org/10.1016/0921-8181(95)00046-1.

Lin, L., Ebtehaj, A.M., Bras, R.L., Flores, A.N., Wang, J., 2015. Dynamical Precipitation Downscaling for Hydrologic applications using WRF 4D-Var Data Assimilation: Implications for GPM Era. J. Hydrometeorol. 16, 811–829. https://doi.org/10.1175/JHM-D-14-0042.1.

Llasat, M.C., Marcos, R., Llasat-Botija, M., Gilabert, J., Turco, M., Quintana-Seguí, P., 2014. Flash flood evolution in North-Western Mediterranean. Atmos. Res. 149, 230–243. https://doi.org/10.1016/j.atmosres.2014.05.024.

Llasat, M.C., Marcos, R., Turco, M., Gilabert, J., Llasat-Botija, M., 2016. Trends in flash flood events versus convective precipitation in the Mediterranean region: the case of Catalonia. J. Hydrol. 541, 24–37. https://doi.org/10.1016/j.jhydrol.2016.05.040.

Lorenzo-Lacruz, J., Coauthors, 2019. Hydro-meteorological reconstruction and geomorphological impact assessment of the October 2018 catastrophic flash flood at Sant Llorenç, Mallorca (Spain). Nat. Hazards Earth Syst. Sci. 19, 2597–2617. https://doi.org/10.5194/nhess-19-2597-2019.

Lu, D., Yong, B., 2018. Evaluation and hydrological utility of the latest GPM IMERG V5 and GSMaP V7 precipitation products over the Tibetan Plateau. Remote Sens. 2022, 10.

Martín-Vide, J.P., Llasat, M.C., 2018. The 1962 flash flood in the Rubí stream (Barcelona, Spain). J. Hydrol. 566, 441–454. https://doi.org/10.1016/j.jhydrol.2018.09.028.

Masson, V., Coauthors, 2013. The SURFEXv7.2 land and ocean surface platform for coupled or offline simulation of earth surface variables and fluxes. Geosci. Model Dev. 6, 929–960. https://doi.org/10.5194/gmd-6-929-2013.

Mastrantonas, N., Bhattacharya, B., Shibuo, Y., Rasmy, M., Espinoza-Dávalos, G., Solomatine, D., 2019. Evaluating the benefits of merging near-real-time satellite precipitation products: a case study in the Kinu Basin Region, Japan. J. Hydrometeor. 20, 1213–1233. https://doi.org/10.1175/JHM-D-18-0190.1.

Michaelides, S., 2013. Advances in precipitation science. Atmos. Res. 119 https://doi.org/10.1016/j.atmosres.2012.11.001.

Michaelides, S., 2019. Editorial for special issue "remote sensing of precipitation". Remote Sens. 11, 389. https://doi.org/10.3390/rs11040389.

Molteni, F., Buizza, R., Palmer, T.N., Petroliagis, T., 1996. The ECMWF ensemble prediction system: methodology and validation. Q. J. R. Meteorol. Soc. 122, 73–119. https://doi.org/10.1002/qj.49712252905.

Mora, J.Á.N., Martín, J.R., García, M.M., de Pablo Davila, F., Rivas Soriano, L., 2016. Climatological characteristics and synoptic patterns of snowfall episodes in the central Spanish Mediterranean area. Int. J. Climatol. 36 (14), 4488–4496.

Neiman, P.J., Ralph, F.M., Moore, B.J., Hughes, M., Mahoney, K.M., Cordeira, J.M., Dettinger, M.D., 2012. The landfall and inland penetration of a flood-producing atmospheric River in Arizona. Part I: observed synoptic-scale, orographic, and hydrometeorological characteristics. J. Hydrometeorol. 14, 460–484. https://doi.org/10.1175/JHM-D-12-0101.1.

Olcina Cantos, J., Hernández Hernández, M., Rico Amorós, A.M., Martínez Ibarra, E., 2010. Increased risk of flooding on the coast of Alicante (Region of Valencia, Spain). Nat. Hazards Earth Syst. Sci. 10, 2229–2234. https://doi.org/10.5194/nhess-10-2229-2010.

Owens, R.G., Hewson, T.D., 2018. ECMWF Forecast User Guide. ECMWF, Reading. https://doi.org/10.21957/m1cs7h.

Palmer, Tim, 2019. The ECMWF ensemble prediction system: looking back (more than) 25 years and projecting forward 25 years. Q. J. R. Meteorol. Soc. 145 (2019), 12–24. https://doi.org/10.1002/qj.3383.

Pinty, J.P., Jabouille, P., 1998. "a Mixed-Phase Cloud Parameterization for Use in Mesoscale Non-hydrostatic Model: Simulations of a Squall Line and of Orographic Precipitations." Conf. On Cloud Physics. American Meteorological Society, Everett, WA.

Pu, Z., Yu, C., Tallapragada, V., Jin, J., McCarty, W., 2019. The Impact of Assimilation of GPM Microwave Imager Clear-Sky Radiance on Numerical Simulations of Hurricanes Joaquin (2015) and Matthew (2016) with the HWRF Model. Mon. Weather Rev. 147, 175–198. https://doi.org/10.1175/MWR-D-17-0200.1.

Ramis, C., Romero, R., Homar, V., 2009. The severe thunderstorm of 4 october 2007 in mallorca: an observational study. Nat. Hazards Earth Syst. Sci. 9, 1237–1245. https://doi.org/10.5194/nhess-9-1237-2009.

Ravazzani, G., Amengual, A., Ceppi, A., Homar, V., Romero, R., Lombardi, G., Mancini, M., 2016. Potentialities of ensemble strategies for flood forecasting over the Milano urban area. J. Hydrol. 539, 237–253. https://doi.org/10.1016/j.jhydrol.2016.05.023.

Retalis, A., Katsanos, D., Tymvios, F., Michaelides, S., 2018. Validation of the first years of GPM operation over Cyprus. Remote Sens. 10 https://doi.org/10.3390/rs10101520.

Romero, R., Martín, A., Homar, V., Alonso, S., Ramis, C., 2005. Predictability of prototype flash flood events in the Western Mediterranean under uncertainties of the precursor upper-level disturbance: the HYDROPTIMET case studies. Nat. Hazards Earth Syst. Sci. 5 (4), 505–525.

Romero, R., Ramis, C., Homar, V., 2015. On the severe convective storm of 29 October 2013 in the Balearic Islands: Observational and numerical study. Q. J. R. Meteorol. Soc. 141, 1208–1222. https://doi.org/10.1002/qj.2429.

Seity, Y., Brousseu, P., Malardel, S., Hello, G., Benard, P., Bouttier, F., Lac, C., Masson, V., 2011. The AROME-France convective-scale operational model. Mon. Weather Rev. 139, 976–991. https://doi.org/10.1175/2010MWR3425.1.

Tapiador, F.J., Navarro, A., García-Ortega, E., Merino, A., Sánchez, J.L., Marcos, C., Kummerow, C., 2020. The Contribution of Rain Gauges in the Calibration of the IMERG Product: Results from the First Validation over Spain. J. Hydrometeorol. 21 (2), 161–182. https://doi.org/10.1175/JHM-D-19-0116.1.

Toté, C., Patricio, D., Boogaard, H., Van der Wijngaart, R., Tarnavsky, E., Funk, C., 2015. Evaluation of satellite rainfall estimates for drought and flood monitoring in mozambique. Remote Sens. 7, 1758–1776. https://doi.org/10.3390/rs70201758.

Valenzuela, P., Iglesias, M., Domínguez-Cuesta, M.J., García, M.A.M., 2018. Meteorological patterns linked to landslide triggering in Asturias (NW Spain): a preliminary analysis. Geosciences (Switzerland) 8 (1).

van der Veen, S.H., 2012. Improving NWP model cloud forecasts using meteosat second-generation imagery. Mon. Weather Rev. 141, 1545–1557. https://doi.org/10.1175/MWR-D-12-00021.1.

Watters, D., Battaglia, A., Mroz, K., Tridon, F., 2018. Validation of the GPM version-5 surface rainfall products over Great Britain and Ireland. J. Hydrometeorol. 19, 1617–1636. https://doi.org/10.1175/JHM-D-18-0051.1.

Wilks, D.S., 2011. Statistical Methods in the Atmospheric Sciences. Academic Press. ISBN: 9780123850225. URL: https://www.sciencedirect.com/bookseries/international-geophysics/vol/100.

Wu, H., Adler, R.F., Hong, Y., Tian, Y., Policelli, F., 2012. Evaluation of global flood detection using satellite-based rainfall and a hydrologic model. J. Hydrometeorol. 13, 1268.1284.

Wu, H., Adler, R.F., Tian, Y., Huffman, G.J., Li, H., Wang, J., 2014. Real-time global flood estimation using satellite-based precipitation and a coupled land surface and routing model. Water Resour. Res. 50, 2693.2717. https://doi.org/10.1002/2013WR014710.

Yuan, F., Zhang, L., Wah Win, K.W., Ren, L., Zhao, C., Zhu, Y., Jiang, S., Liu, Y., 2017. Assessment of GPM and TRMM multi-satellite precipitation products in streamflow simulations in a data sparse mountainous watershed in Myanmar. Remote Sens. 9. https://doi.org/10.3390/rs9030302.

Zhou, T., Nijssen, B., Huffman, G.J., Lettenmaier, D.P., 2014. Evaluation of real-time satellite precipitation data for global drought monitoring. J. Hydrometeorol. 15, 1651–1660. https://doi.org/10.1175/JHM-D-13-0128.1.

Zhuge, X.-Y., Yu, F., Zhang, C.-W., 2011. Rainfall retrieval and nowcasting based on multispectral satellite images. Part I: retrieval study on daytime 10-minute rain rate. J. Hydrometeorol. 12, 1255–1270. https://doi.org/10.1175/2011JHM1373.1.

Zsótér, E., 2006. Recent developments in extreme weather forecasting. ECMWF Newsletter 107 (107), 8–17.

Zsótér, E., Pappenberger, F., Richardson, D., 2015. Sensitivity of model climate to sampling configurations and the impact on the Extreme Forecast Index. Meteorol. Appl. 22 (2), 236–247.